Divergent Adsorption-Dependent Luminescence of Amino-Functionalized Lanthanide Metal-Organic Frameworks for Highly Sensitive NO$_2$ Sensors

Arturo Gamonal,[†] Chen Sun,[†] A. Lorenzo Mariano,[‡] Estefania Fernandez-Bartolome,[†] Elena Guerrero-SanVicente,[†] Bess Vlaisavljevich,[∞] Javier Castells-Gil,[‖] Carlos Marti-Gastaldo,[‖] Roberta Poloni,[‡]* Reinhold Wannemacher,[†]* Juan Cabanillas-Gonzalez [†]* and Jose Sanchez Costa [†]*

[†] IMDEA Nanociencia, Ciudad Universitaria de Cantoblanco 28049, Madrid. Spain

[‡] SIMaP laboratory; CNRS, University Grenoble Alpes; Grenoble. France.

[∞] University of South Dakota; 414 E Clark Street, Vermillion, SD, 57069, USA.

[‖] Instituto de Ciencia Molecular, Universitat de Valencia, Catedrático José Beltrán 2, 46980 Paterna, Spain

AUTHOR INFORMATION

Corresponding Author

*Email: jose.sanchezcosta@imdea.org; juan.cabanillas@imdea.org; reinhold.wannemacher@imdea.org; roberta.poloni@grenoble-inp.fr

Table of Contents

Sec 1) Experimental details

Materials. Chemicals and reagents (amino terephtalic acid, $LnNO_3 \cdot xH_2O$ (Eu, Tb and Gd) and N,N´-dimethylformamide) were purchased from commercial suppliers and used as received.

Physical measurements.

- FT-IR spectra were recorded as neat samples in the range 400-4000 cm^{-1} on a Bruker Tensor 27 ATR-Spectrometer.
- TGA was performed using a TA Instrument TGAQ500 with a ramp of 2 ºC/min under air and nitrogen from 30 to 500 ºC.
- Elemental analyses (C, H and N) were performed on a LECO CHNS-932 Analyzer at the "Servicio Interdepartamental de Investigación (SIdI)" at Autónoma University of Madrid.
- Crystal Structure Determination: The data were collected with an orange block crystal of 1 with a Bruker APEX II CCD diffractometer at the Advanced Light Source beamline 11.3.1 at Lawrence Berkeley National Laboratory from a silicon (111) mono- chromator (T = 100, K, λ = 0.7749 Å). The crystal was taken directly from its solution, mounted with a drop of Paratone-N oil and immediately put into the cold stream of dry N_2 on the goniometer. The structure was solved by direct methods and the refinement on F^2 and all further calculations were carried out with the SHELX-TL suite.
- Powder X-ray diffratograms were obtained by using a Panalytical X'Pert PRO diffractometer (Cu-Kα1 X-radiation, λ1=1.5406 Å) with parallel-beam collimator, graphite secondary monochromator and Xenon detector. Theta / 2 theta sweep has been carried out from 5º to 90º range with an angular increase of 0,04º. Diffraction patterns were recorded at room temperature.
- Low temperature PL measurements were carried out with the powder samples mounted in an aluminium support behind a quartz window. The assembly was fixed to the sample holder of a Magnex needle valve optical cryostat and cooled down with nitrogen gas. The sample space was then filled with liquid nitrogen (LN_2), which was subsequently pumped down to 65 K. The pressure in the sample space was then raised to ambient conditions with dry nitrogen in order to remove the bubbles. Measurements were performed during the very slow warm up of the LN_2 surrounding the sample. A TEEM Photonics Nd:YAG laser (λ=355 nm), delivering pulses of 300 ps duration at repetition rates from single shot to 1 kHz, a Picoquant LDH−D−C−405 pulsed diode laser (λ=405 nm, FWHM<49ps) and a 405 nm cw laser diode module with TTL modulation up to 20 kHz were employed as pumping sources, according to the requirements of the measurements. The photoluminescence was detected under 90° by means of an Acton Research SP2500 spectrometer (f = 500 mm) equipped with a Princeton Instruments Spec-10 liquid nitrogen cooled back-illuminated deeply depleted CCD for the acquisition of PL spectra and a PicoQuant PMA 06 low dark current hybrid photomultiplier for PL decay measurements. Gated phosphorescence spectra were acquired after the excitation pulse using suitable external triggering of the Nd:YAG laser and the CCD at a minimum delay of about 30 ms.
- Trigger pulses for the laser and the CCD camera were provided by a Stanford Research Systems DG645 pulse and delay generator with 5 ps resolution. PL decay measurements were carried out by the time correlated single photon counting (TCSPC) technique using either a Picoquant HydraHarp 400 electronics with 1 ps resolution or a Picoquant TimeHarp 260 nano TCSPC electronics with 1 ns resolution. The decay time fitting procedure was carried out using the Fluofit software (PicoQuant).
- Room temperature measurements in a flow of synthetic air and 5 ppm NO_2 in synthetic air, respectively, were performed in a quartz cell with the powder samples placed in an aluminium support behind a gas-permeable copper TEM grid. The gas flow could be controlled via flow meters equipped with valves. PL spectra and PL lifetimes were measured as described above.

Sec 2) Synthesis of 1, 2 and 3

General Procedure: A solution of 0.23 mmol of $Ln(NO_3)_3 \cdot 5H_2O$ (Ln= Tb (**1**), Eu (**2**), Gd (**3**)) in 10 mL of N,N´-dimethylformamide (DMF) and a solution of amino terephtalic acid (N-H_2BDC) (62 mg, 0.34 mmol) in DMF (10 mL) were mixted in a glass tube (Duran culture tube, diameter 18 mm, height 180 mm). The tube was sealed and placed in an oven at 120 °C for 20 h, resulting in the formation of single crystals. The crystals were filtered, washed with DMF (~5 mL), and dried in the vacuum oven for 15 min. It has to be mentioned here that the MOFs most likely lose DMF solvent molecules during the drying and pick up atmospheric water upon air exposure. Yield: 82%, 73%, 80% for **1**, **2** and **3**, respectively.

Elemental analysis found for $\{[Tb_2(NBDC)_3(DMF)_4] \cdot DMF\}_\infty$ (**1**); C, 38.41; H, 4.28; N, 9.15%. Calcd: C, 38.37; H, 4.13; N, 9.18%. Selected IR data (Neat): 3443 (w) ν(OH), 3339 (w) ν(NH), 2930 (w) ν(CH), 1672 (m) ν(CO), 1646 (m) vas(COO), 1546 (m) ν(CdC), 1497 (m) vs(COO), 1416 (m) ν(CO), 1374 (s) ν(CN), 1251 (m) ν(CO), 770 (s) δ(OCO), 676 (s) δ(dCH) cm^{-1}.

Elemental analysis found for $\{[Eu_2(NBDC)_3(DMF)_2] \, 0.5DMF \, 2H_2O\}_\infty$ (**2**); C, 35.41; H, 3.55; N, 6.97%. Calcd: C, 35.49; H, 4.02; N, 7.23%. Selected IR bands (Neat, ν/cm^{-1}): 3455 (w) ν(OH),3341 (w) ν(NH), 2932 (w) ν(CH), 1670 (m) ν(CO), 1646 (m)vas(COO), 1544 (m) ν(CdC), 1496 (m) Vs(COO), 1416 (m) ν(CO), 1375 (s) ν(CN), 1251 (m) ν(CO), 770 (s) δ(OCO), 672 (s) δ(dCH)cm^{-1}. The crystals were analyzed by single-crystal X-ray diffraction and by X-ray powder diffraction.

Elemental analysis found for $\{[Gd_2(NBDC)_3(DMF)_4] \cdot DMF\}_\infty$ (**3**); C, 38.15; H, 4.21; N, 9.10%. Calcd: C, 38.14; H, 3.97; N, 8.90%. Selected IR bands (Neat, ν/cm^{-1}): 3445 (w) ν(OH), 3344 (w) ν(NH), 2931 (w) ν(CH), 1668 (m) ν(CO), 1649 (m) vas(COO), 1540 (m) ν(CdC), 1496 (m) Vs(COO), 1417 (m) ν(CO), 1373 (s) ν(CN), 1252 (m) ν(CO), 770 (s) δ(OCO), 676 (s) δ(dCH) cm^{-1}.
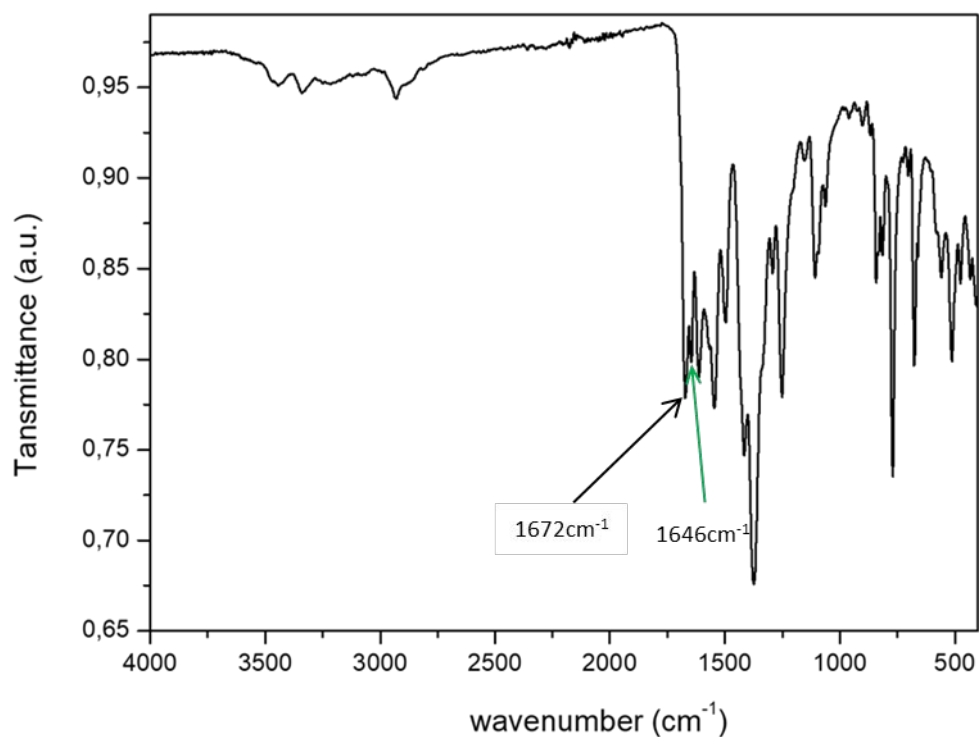
Sec 3) Fourier Transform Infrared spectra

Figure S1. Infrared Spectrum of **1**·2DMF {[Tb$_2$(N-BDC)$_3$(DMF)$_4$]$_\infty$·2DMF}

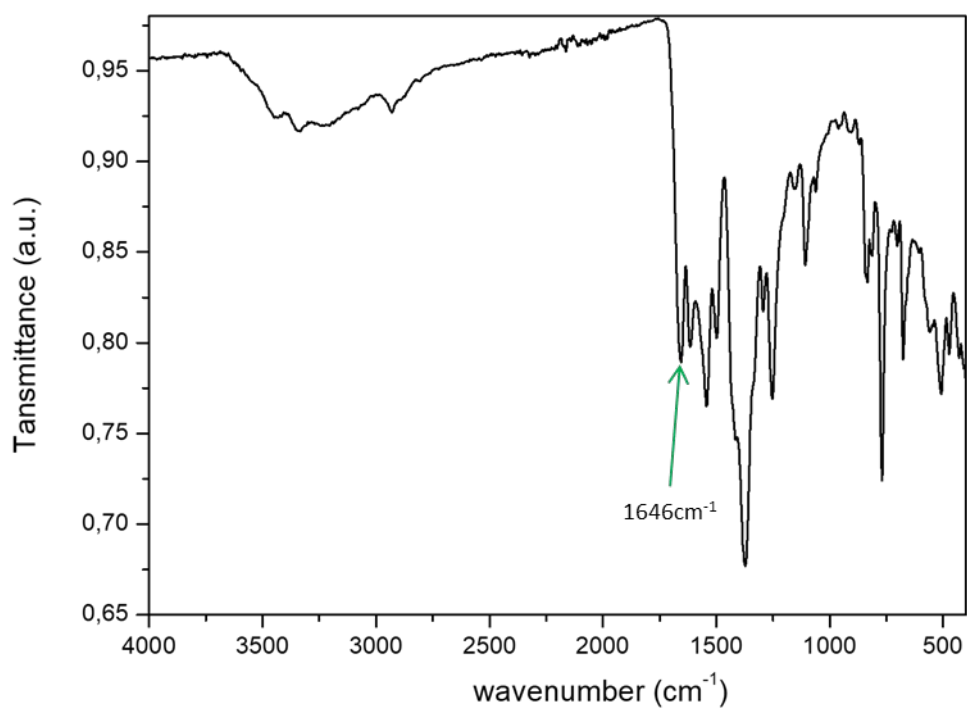**Figure S2.** Infrared Spectrum of **1**{[Tb$_2$(N-BDC)$_3$(DMF)$_4$]$_\infty$}, after activation with dry air. Notice the disappearance of the band at 1672 cm^{-1} corresponding to crystallization of DMF
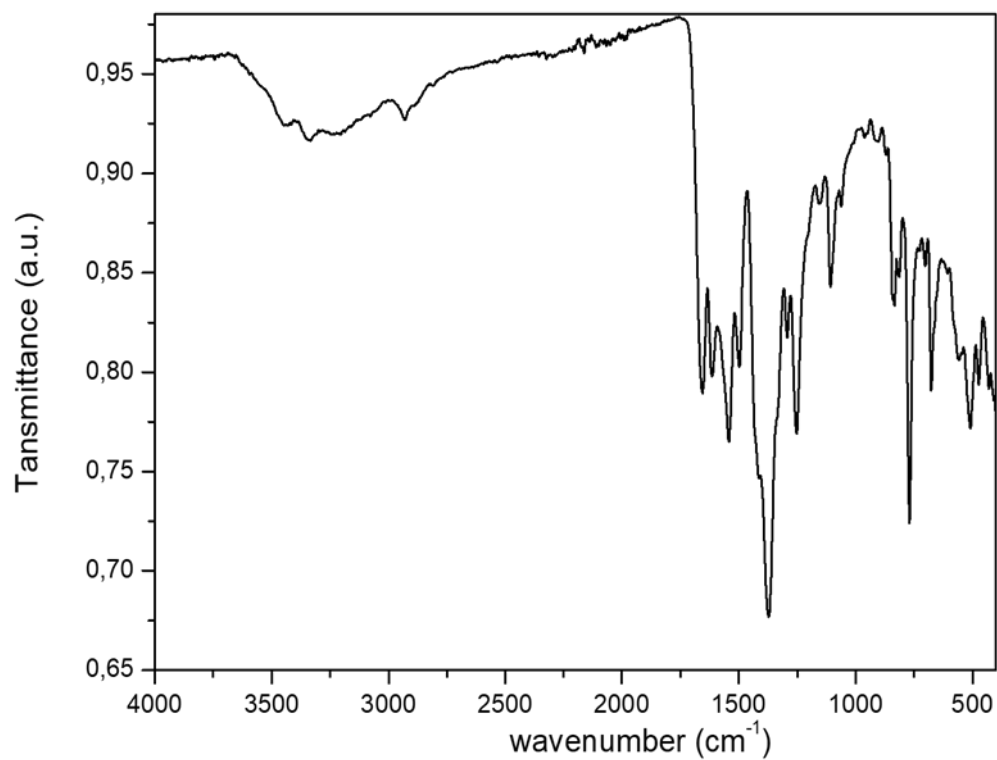
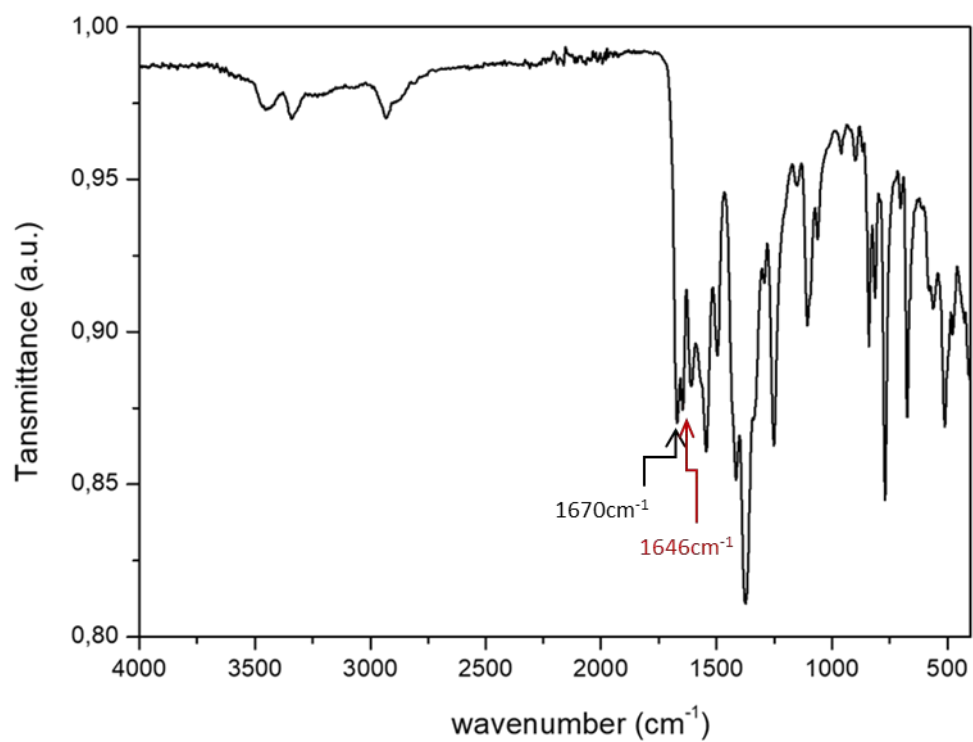**Figure S3.** Infrared Spectrum of **1**{[Tb$_2$(N-BDC)$_3$(DMF)$_4$]$_\infty$} after exposure to 5ppm NO$_2$.

1670cm^{-1}

1646cm^{-1}

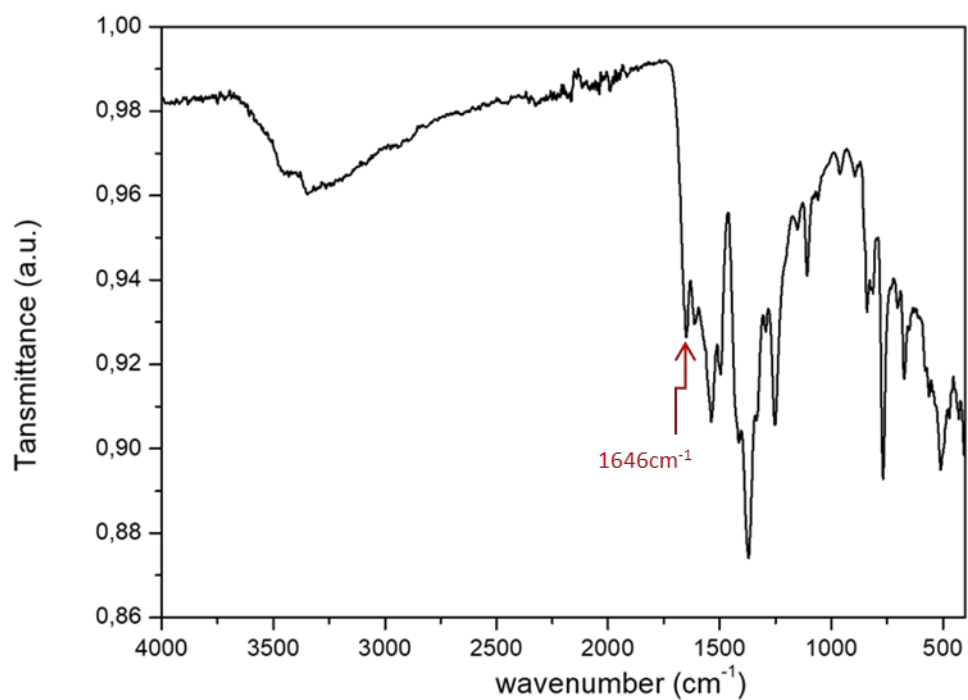**Figure S4.** Infrared Spectrum of compound **2**·2DMF {[Eu$_2$(N-BDC)$_3$(DMF)$_4$]$_\infty$·2DMF}

Figure S5. Infrared Spectrum of **2**{[Eu$_2$(N-BDC)$_3$(DMF)$_4$]$_\infty$}, after activation with dry air of **2**·2DMF. Note that the band at 1670 cm^{-1} corresponding to DMF disappears

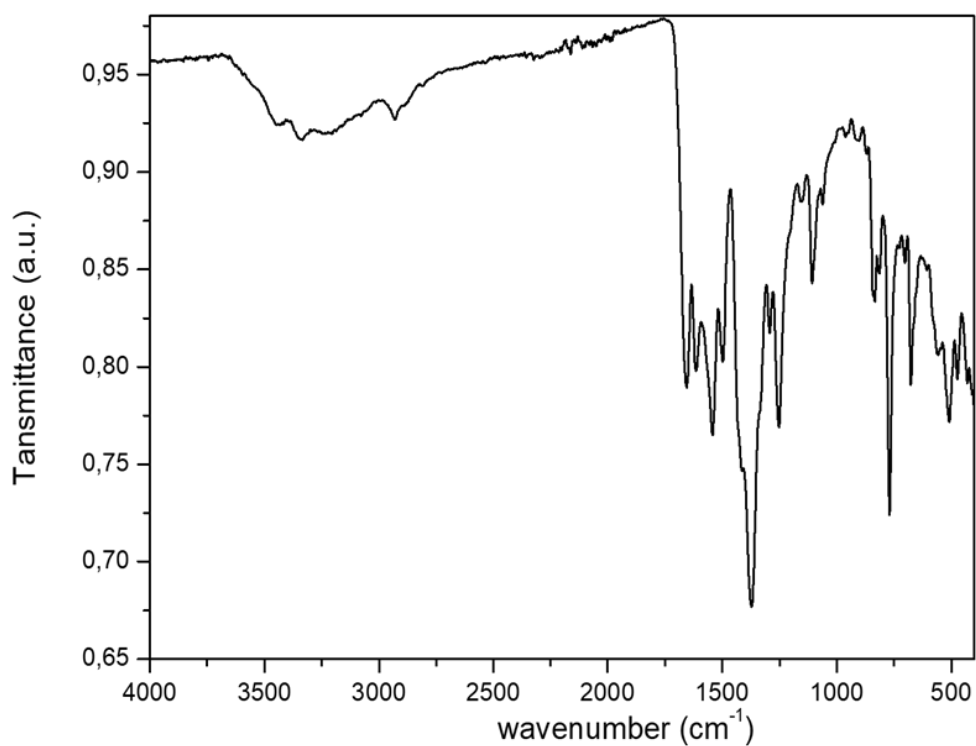**Figure S6.** Infrared Spectrum of **2** {[Eu$_2$(N-BDC)$_3$(DMF)$_4$]$_\infty$}after exposure to 5ppm NO$_2$.
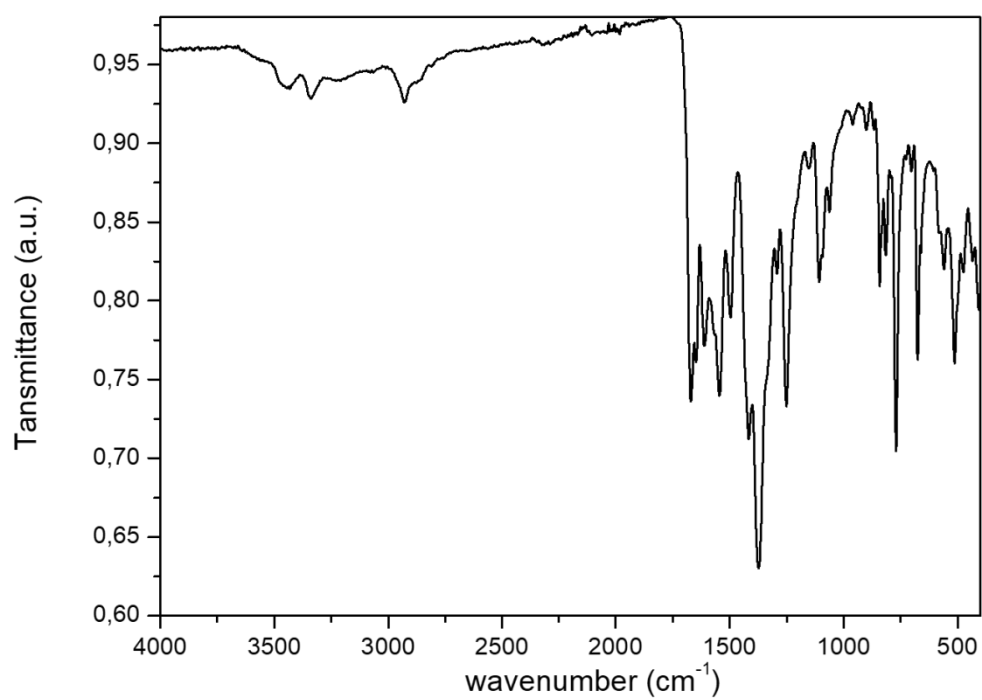
Figure S7. Infrared Spectrum of **3**

Sec 4) Thermogravimetric analysis of 1 and 2
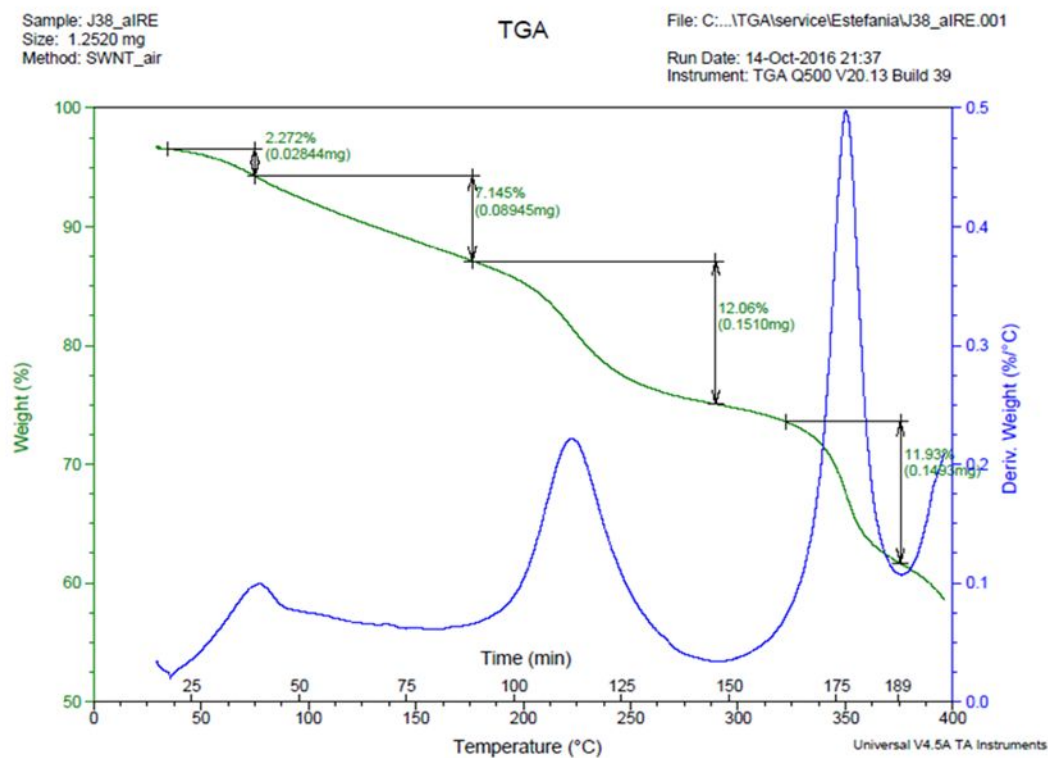
Figure S8. Thermogravimetric analysis of **1** run in air at a heating rate of 2ºC min^{-1}
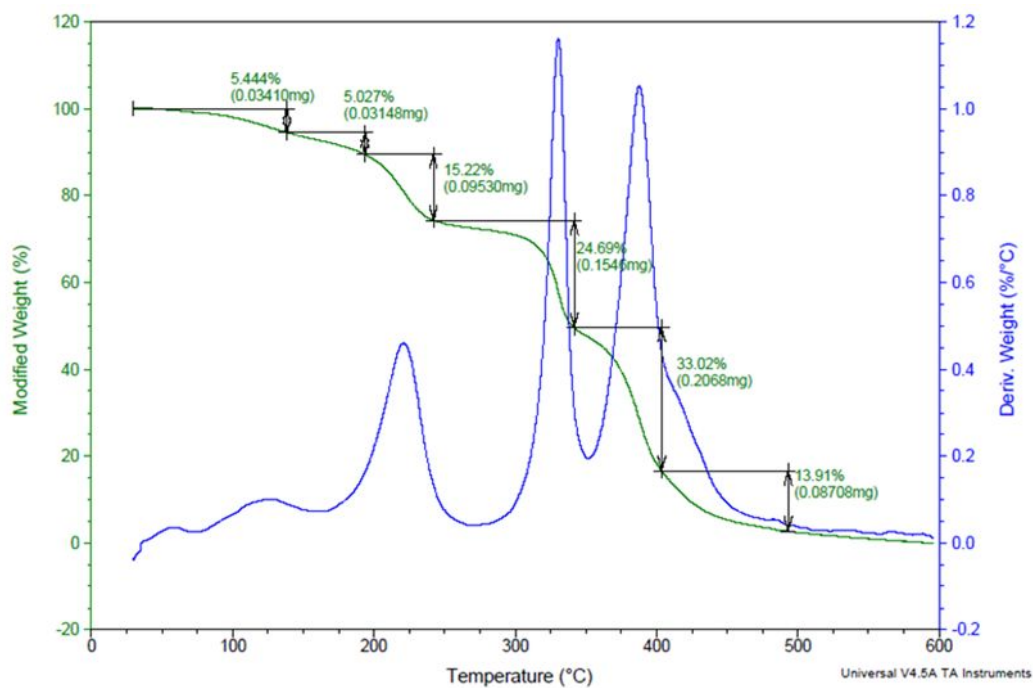
Figure S9. Thermogravimetric analysis of **2** run in air at a heating rate of 2ºC min^{-1}.

Sec 5) X-ray Powder Diffraction (XRD) of 2
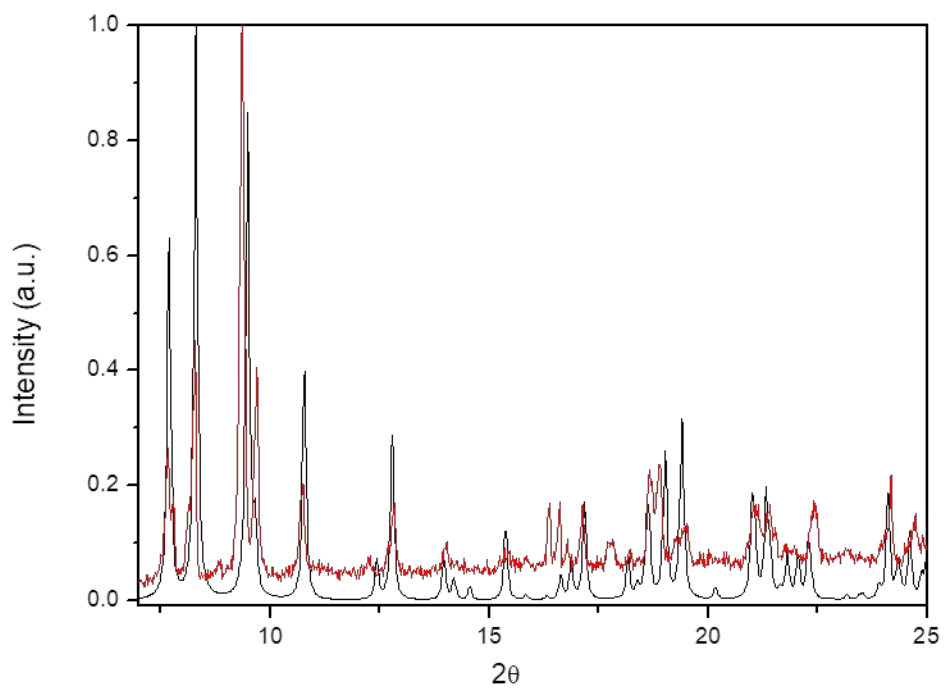
Figure S10. PXRD superimposed spectra of **2.** The spectrum calculated from single crystal diffraction using MERCURY software (black) and the PXRD experimentally obtained from the synthesis (red).

Sec 6) Normalized PLE and PL spectra for 1, 2 and 3
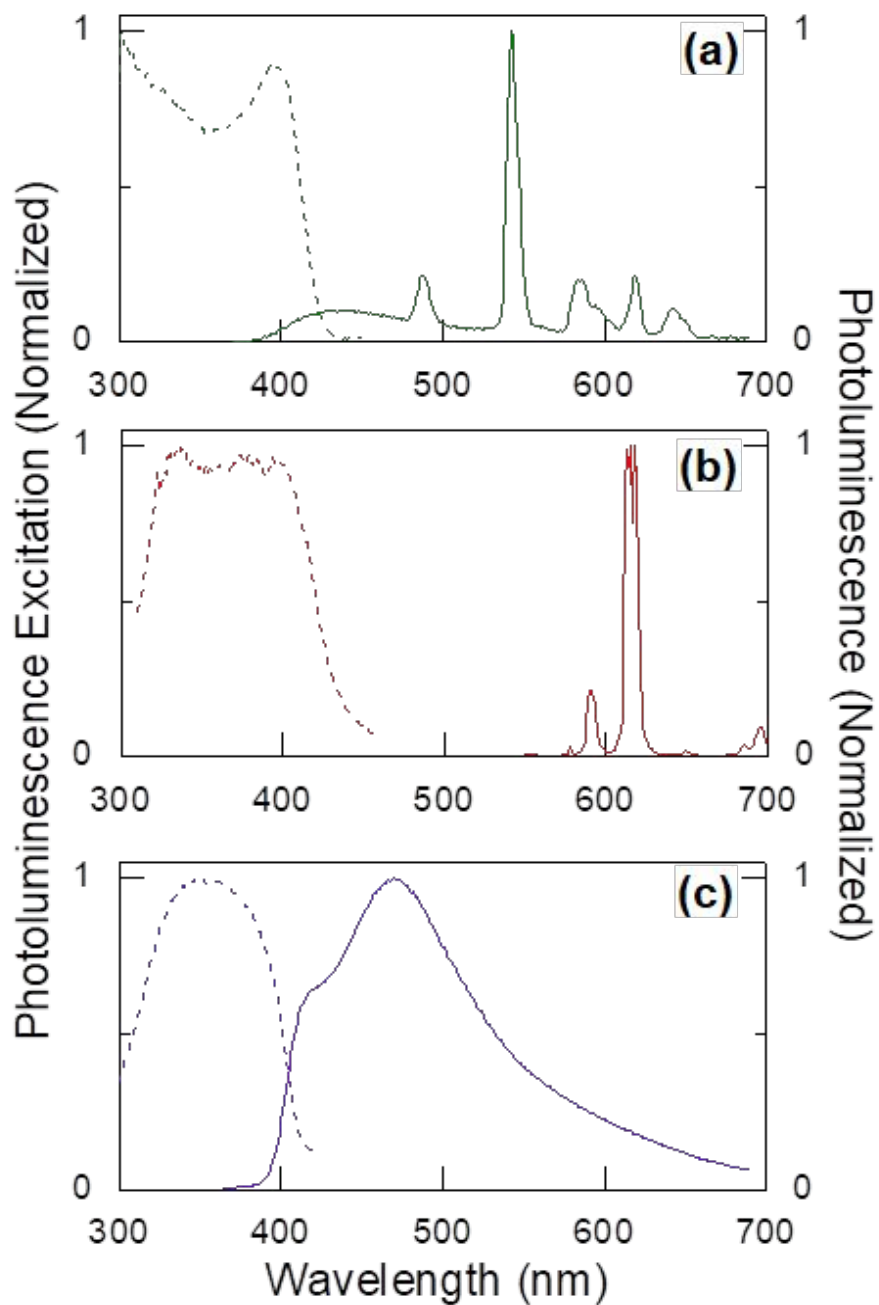
Figure S11. Normalized PLE (dashed line) and PL spectra (solid line) of **1** (a) **2** (b) and **3** (c) at room temperature. PL spectra were excited at 350 nm for **1**, **2** and **3**. PLE was detected at 543 nm, 614 nm and 465 nm in **1**, **2** and **3** respectively.

Sec 7) Photoluminescence study at low temperature (65 K) of the free ligand and 3 (Gd-MOF).
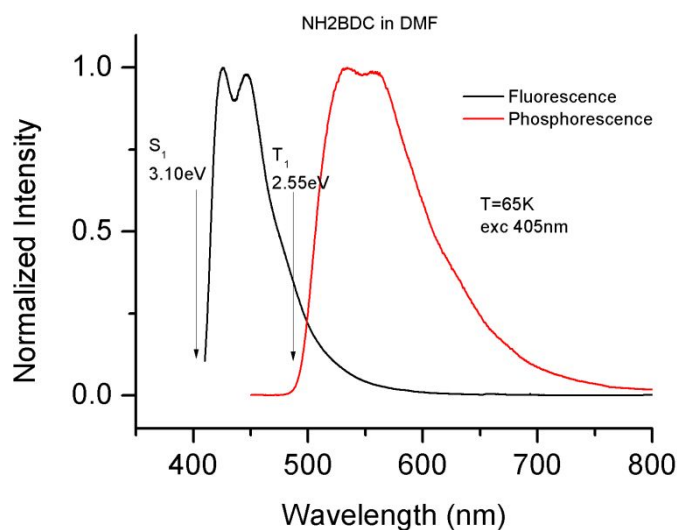
Figure S12. Fluorescence and phosphorescence spectra of the free ligand (NH_2BDC) in DMF at 65K. Excitation wavelength λ_{exc}=405 nm

Figure S13. Fluorescence decay of the free ligand (NH_2BDC) in DMF at 65K detected at 426 nm, λ_{exc}=405 nm, ν_{rep} = 2.5 MHz

| Parameter	Value	Conf. Lower	Conf. Upper	Conf. Estimation
A_1 [Cnts]	7991.8	-48.5	+48.5	Fitting
τ_1 [ns]	14.4055	-0.0609	+0.0609	Fitting
A_2 [Cnts]	1784.7	-95.4	+95.4	Fitting
τ_2 [ns]	6.188	-0.354	+0.354	Fitting
Bkgr. Dec [Cnts]	0.869	-0.320	+0.320	Fitting

Intensity-weighted average lifetime: 13.7 ns.

Table S1. Fit of phosphorescence lifetime of the free ligand (NH_2BDC) in DMF at 65K detected at 426 nm, λ_{exc}=405 nm, ν_{rep} = 2.5 MHz

Figure S14. Phosphorescence decay of the free ligand (NH$_2$BDC) in DMF at 65K detected at 550 nm, λ_{exc}=405 nm, ν_{rep} = 0.5 Hz

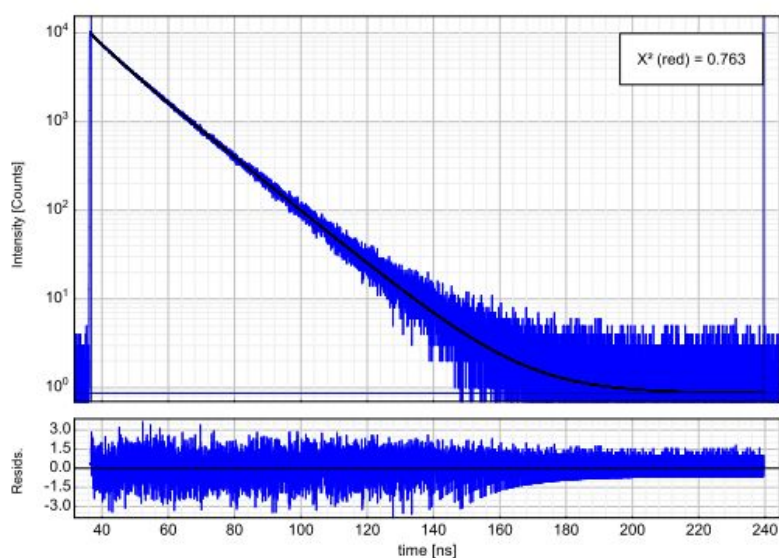| Parameter	Value	Conf. Lower	Conf. Upper	Conf. Estimation
A$_1$ [Cnts]	543.6	-10.5	+10.5	Fitting
τ_1 [s]	0.30686	-0.00438	+0.00438	Fitting
A$_2$ [Cnts]	369.7	-21.5	+21.5	Fitting
τ_2 [s]	0.12939	-0.00779	+0.00779	Fitting
Bkgr. Dec [Cnts]	4.919	-0.752	+0.752	Fitting

Intensity-weighted average lifetime: 0.267 s

Table S2 Fit of phosphorescence lifetime of the free ligand (NH$_2$BDC) in DMF at 65K detected at 550 nm, λ_{exc}=405 nm, ν_{rep} = 0.5 Hz
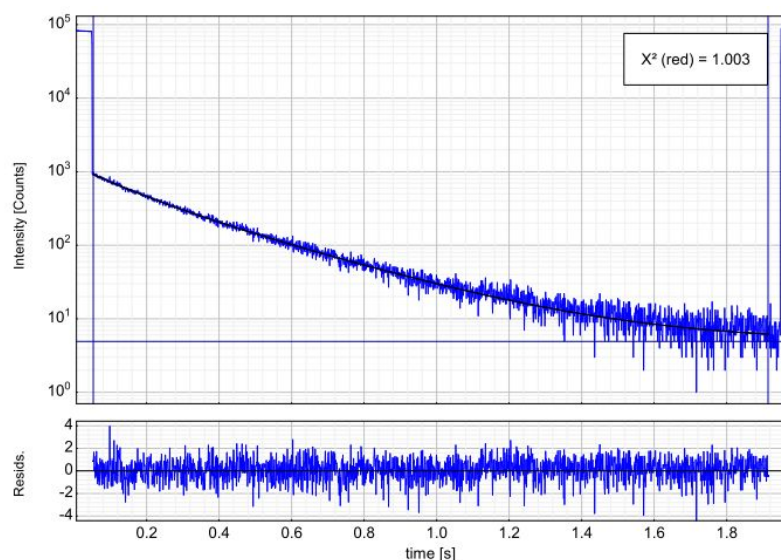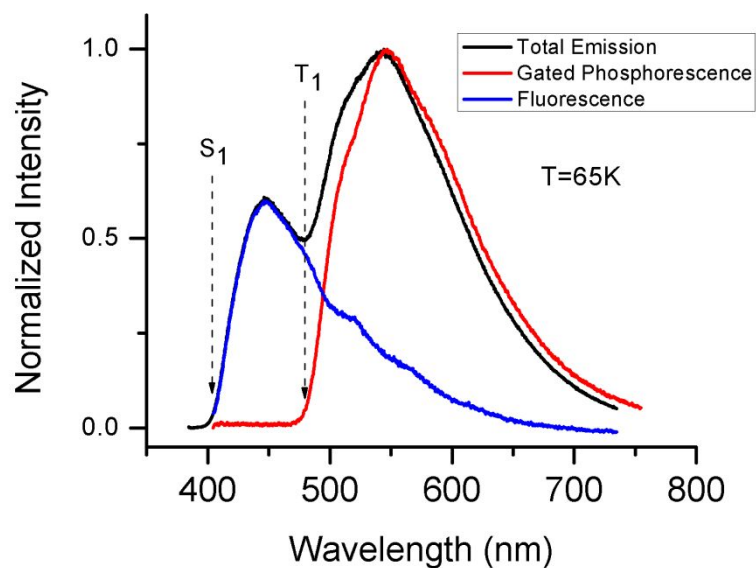

Figure S15. Fluorescence and phosphorescence spectra of **3** measured at T = 65 K, λ_{exc} = 355 nm

S13
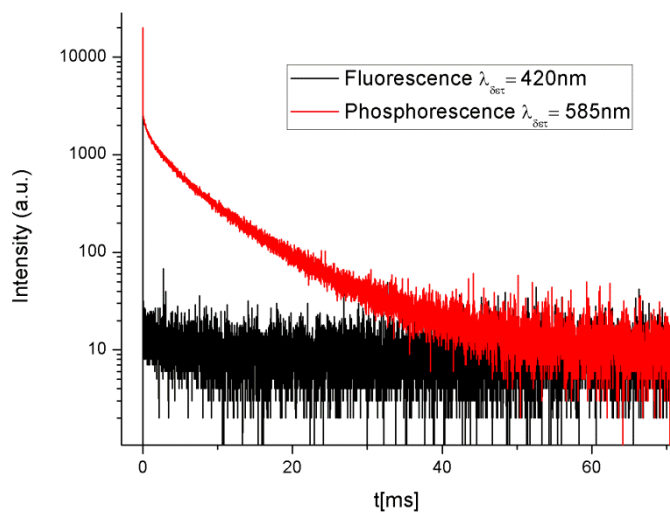
Figure S16. Luminescence decay of **3** {[Gd$_2$(N-BDC)$_3$(DMF)$_4$]$_\infty$} recorded at 65K, λ_{exc}=355 nm.

Parameter	Value	Conf. $_{Lower}$	Conf. $_{Upper}$	Conf. $_{Estimation}$
A$_1$ [Cnts]	567.0	-14.9	+14.9	Fitting
τ_1 [ms]	9.995	-0.186	+0.186	Fitting
A$_2$ [Cnts]	984.6	-36.8	+36.8	Fitting
τ_2 [ms]	3.792	-0.135	+0.135	Fitting
A$_3$ [Cnts]	686	-113	+113	Fitting
τ_3 [ms]	0.677	-0.139	+0.139	Fitting
Bkgr. $_{Dec}$ [Cnts]	9.043	-0.932	+0.932	Fitting

Table S3. Fit of phosphorescence lifetime in **3** measured at λ_{det} = 585 nm and at T = 65 K.

S14

Sec 8) Sensing dilution experiment and detection limit
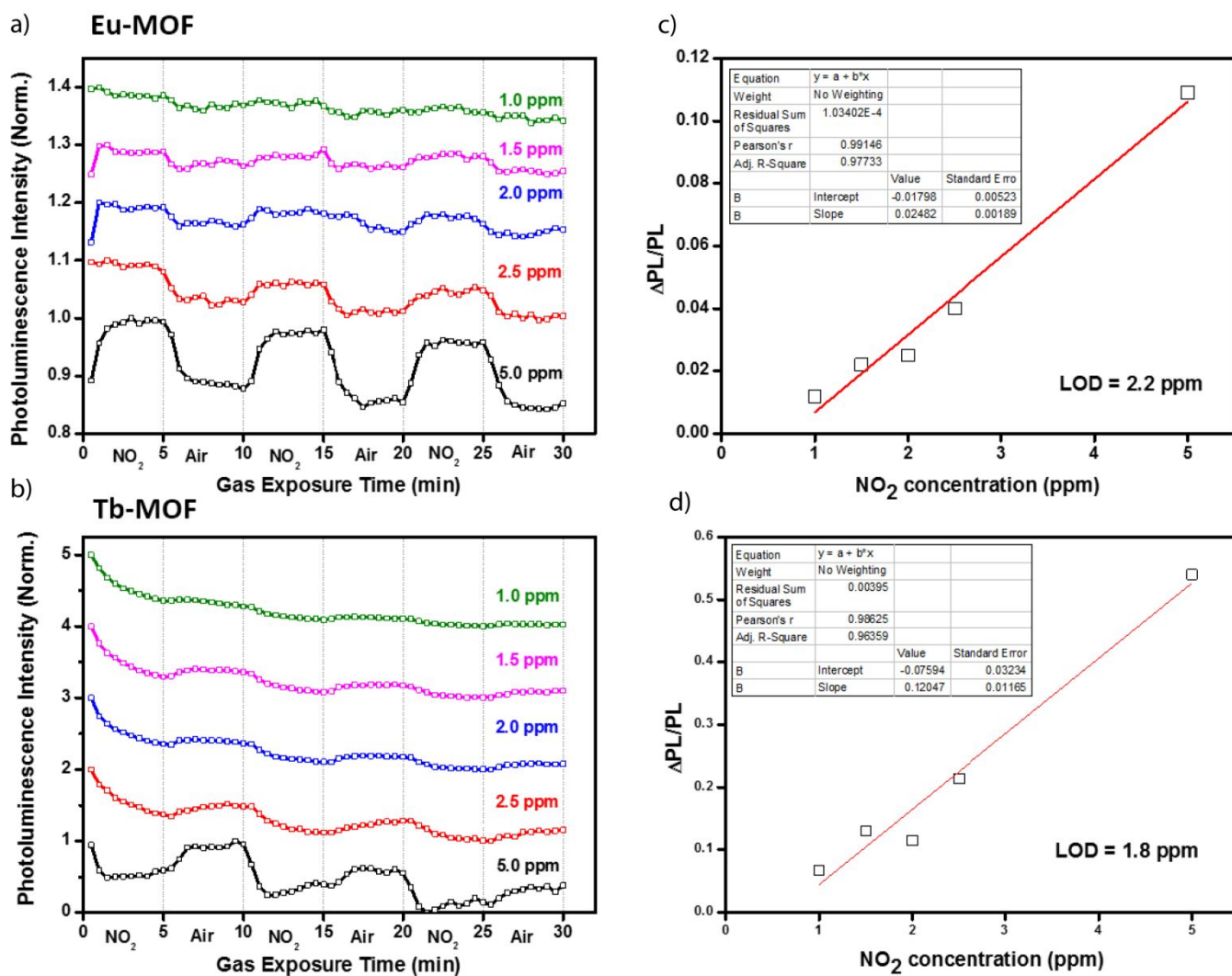
Figure S17. Normalized PL kinetics of Eu-MOF at 615 nm (a) and Tb-MOF at 543 nm (b) upon 3 NO_2-air cycles with 5 different NO_2 contents. The normalized kinetics at different NO_2 concentrations were offset by 0.1 in (a) and by 1 in (c). Relative PL change in Eu-MOF (b) and Tb-MOF (d) as a function of NO_2 concentration. The bold red lines stand for linear fits. The limit of detection (LOD) values were calculated as 3 |σ|/m where σ is the intercept with Y-axis and m the slope of the fit (IUPAC definition).

Sec 9) PL Decays of 1, 2 and 3 at room temperature
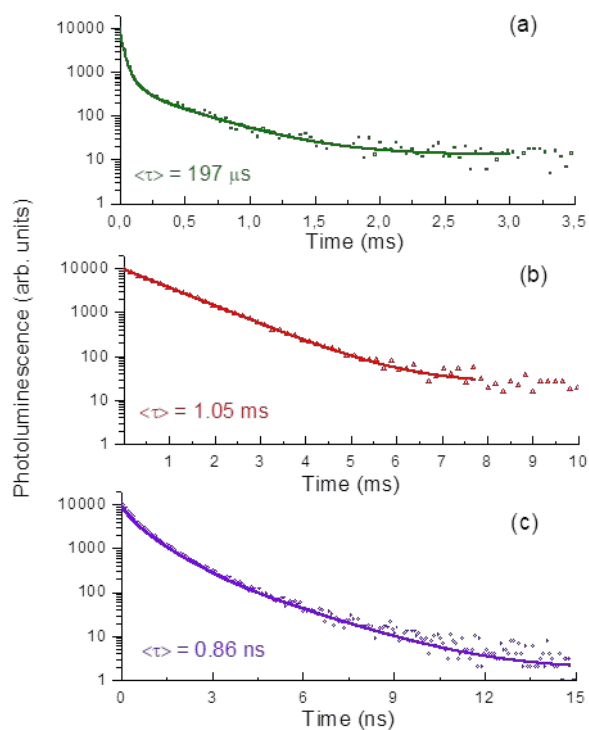
Figure S18. PL decays of **1 (a)**, λ_exc=405 nm, λ_det=543 nm **2 (b)**, λ_exc=405 nm, λ_det=614 nm and **3 (c),** λ_exc=405 nm, λ_det=444 nm in synthetic air at room temperature.
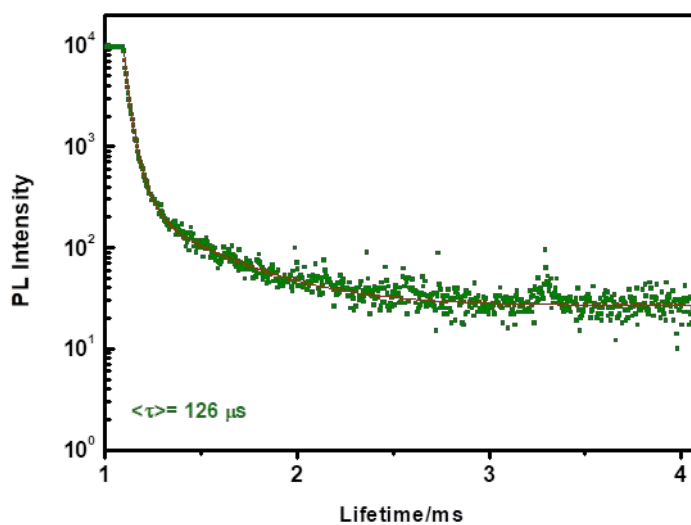
Figure S19. Fluorescence decay of **1** {[Tb₂(N-BDC)₃(DMF)₄] ·2DMF}_∞ in synthetic air plus 5ppm of NO₂ at room temperature., λ_exc=405 nm, λ_det=543 nm.
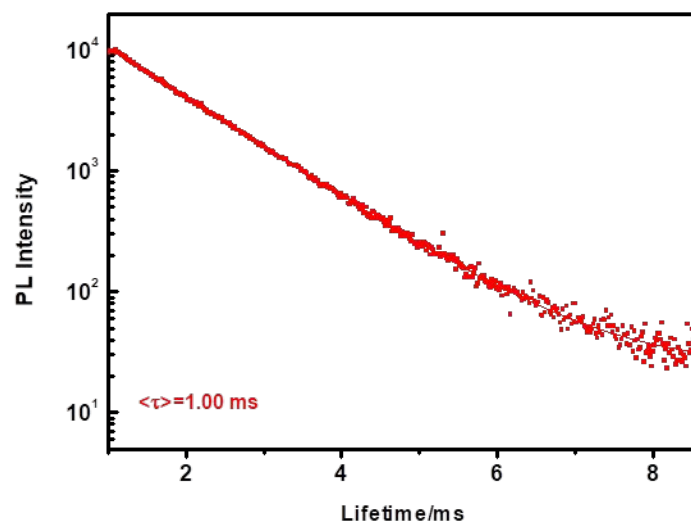
Figure S20. Fluorescence decay of **2** {[Eu$_2$(N-BDC)$_3$(DMF)$_4$] ·2DMF}$_\infty$ in synthetic air plus 5ppm of NO$_2$ at room temperature, λ_{exc}=355 nm, λ_{det}=614 nm.

Sec 10) Adsorption isotherms study:

N_2 and H_2O adsorption isotherms performed ex-situ at 77 and 298 K, respectively, for the Tb-MOF in a Micromeritics 3Flex apparatus. A Micromeritics ISO Controller was used to keep the temperature constant for the H_2O adsorption measurements.

Before the sorption measurements 2·2DMF different activation protocols were tested with the intention of removing the DMF not coordinated to the metal centres by using two different method: i) flowing N_2 during 30 minutes (similar to the sensing procedure) and ii) by solvent exchange with hexane for several days, in which the liquid part was exchanged by fresh hexane 3 times every day, followed by mild heating at 60ºC under vacuum for at least 12 h. The results using both methodologies are almost identical (see Figure for methodology ii).

These experiments reveal that no N_2 can be adsorbed in the framework whereas only a small adsorption of H_2O (7.09 mmol g^{-1} respectively) is observed at room temperature likely due to the adsorption of water molecules onto the external surface of the material.

Figure S21. N_2 (blue dots) and H_2O (green dots) adsorption isotherms for 2.

Sec 11) Ab initio calculations

DFT calculations

All DFT calculations were performed with the PWscf.x utility of QuantumESPRESSO .[1] Since it is now well known that the 4f can be considered as core electrons when dealing with chemical bond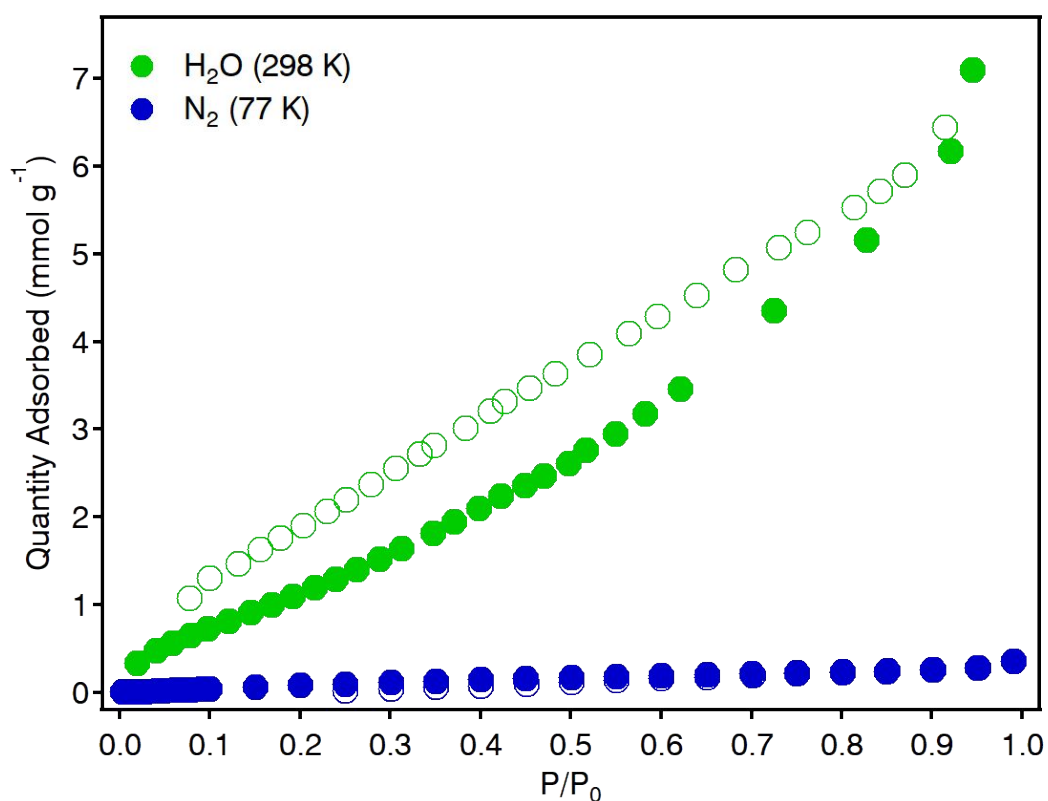ing, we employ the Rappe-Rabe-Kaxiras-Joannopolous ultrasoft pseudopotential for Tb and Eu generated with 4f electrons in the core and available in the PSlibrary. Since non-local dispersion interactions are expected for NO_2 bound to the Eu-MOF, we employ the rev-vdW-DF2 functional.[2] With respect to the previous vdW-DF functionals originally developed by Langreth and Lundqvist,[3,4] this functional significantly improves on the prediction of bond distance and binding energy of H-bond systems, which is, as we will see below, critical in this case.

The wavefunction and charge density cutoff s were set to 60 Ry and 540 Ry, respectively. The geometrical optimizations were performed until all components of forces on the atoms are less than 0.025 eV/Ang and the stress less than 0.015 kbar. The Brillouin zone sampling was performed using the Γ point only. We find the inclusion of spin polarization necessary for the description of the NO_2 binding mechanism. Then, first we fully optimize the geometries with non-spin polarization (atomic positions and cell) and then we add spin polarization and perform the atomic optimization only (stress calculations non implemented with non-local vdW functionals and spin polarization).

NO$_2$ binding

In our simulations, the P-1 symmetry is broken because of the loss of fractional occupancy of NH_2: the crystallographic data report 4 inequivalent Wyckoff positions for N within the primitive cell (two positions with 0.5 occupancy and two with 0.25). We explicitly studied the 8 inequivalent configurations (the 16 total combinations are reduced to 8 by centro-symmetry). In **Figure S22**, we illustrate the location of the amino groups from crystallographic data by colouring the C atoms which are coordinated to the N of NH_2. Equivalent positions according to the available crystallographic data are labelled with the primed number.[5] Since only three ligands are contained in the primitive cell, the same colour is used for periodic images for clarity. The probability of finding an amine bound to each carbon in positions 1, 2, 3, 4 is reported to be 25% while for both 5, 6 and 7, 8 is 50%. For each configuration three amine groups are present in the unit cell so that the right stoichiometry is achieved and all possible combinations are generated. The description of these configurations is reported in **Table S4**.

Configuration	1	2	3	4	5	6	7	8
Amine position	2-3-4	1'-3-4	1-3-4	2'-3-4	2-3-4'	1'-3-4'	1-3-4'	2'-3-4'

Table S4. Description of the 8 inequivalent configurations computed in this work. The numbers in the second row refer to carbon sites coordinated to the NH_2 group and shown in Figure S1.
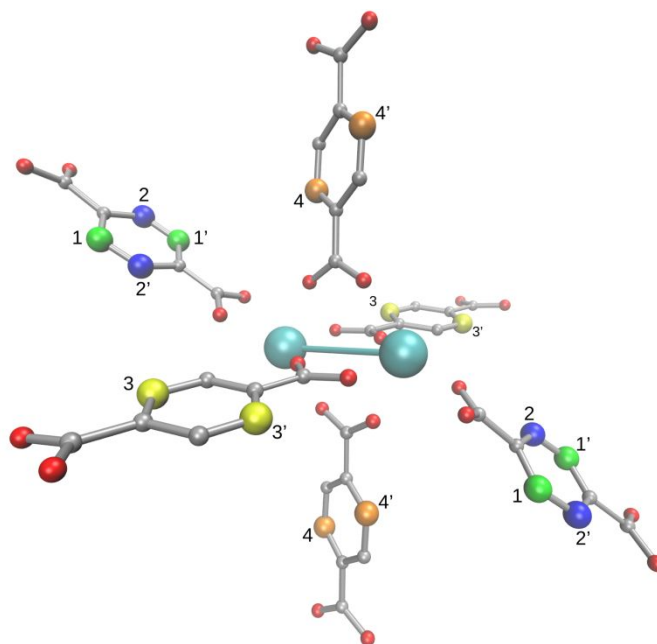

Figure S22. Schematic view of the amine locations within the ligands coordinating the Ln-Ln dimer within the MOF. The 1-4 numbers refer to the 4 inequivalent Wyckoff positions (the prime refers to the same position by symmetry). The same colour is used for periodic images.

For all the cases, a full geometrical optimization is performed by inserting the NH_2 groups in the experimental structure of the bare MOF described above. In order to find the NO_2 binding location, we computed the electrostatic potential energy map of the bare MOF for each configuration, as shown in Figure S23 and placed the NO_2 in regions of attractive electrostatic potential.

This procedure has allowed us to correctly predict, in the past, the location of adsorbate molecules in MOFs in absence of experimental guidance.[6] Here we clearly see regions of positive potential(in red) around the metal and regions of negative potential (in blue) around the ligands O atoms. In every case we find pockets of large negative potential (positive potential energy) near the metal site, between O atoms (see orange pocket in **Figure S23**). We place the N atom of NO_2 in these pockets and perform a full atomic relaxation while testing different initial orientations of NO_2 in each case. In all cases, the final position of NO_2 relaxed in the center of the pore. The potential energy surface is then further explored by rotating systematically the molecule and relaxing the structure. The final configuration consists of a NO_2 molecule hydrogen bonded to one or more neighboring amines, depending on the configuration. The binding configuration and binding energy vary from conFigure 1 to 8 but we find the binding mechanism to be electrostatics, H-bonds and van der Waals in all cases The binding energy varies from a minimum of 0.37 eV (0.37 eV) for conFigure 2 to a maximum value of 0.54 eV (0.57 eV) for conFigure 5 (conFigure 3) for Eu (Tb), as shown in Table S5. To give an estimate of the van der Waals contribution, we computed the binding energy using PBE, for configuration 1, and obtained 0.31 eV, while the rev-vdW-DF2 gives 0.48 eV.
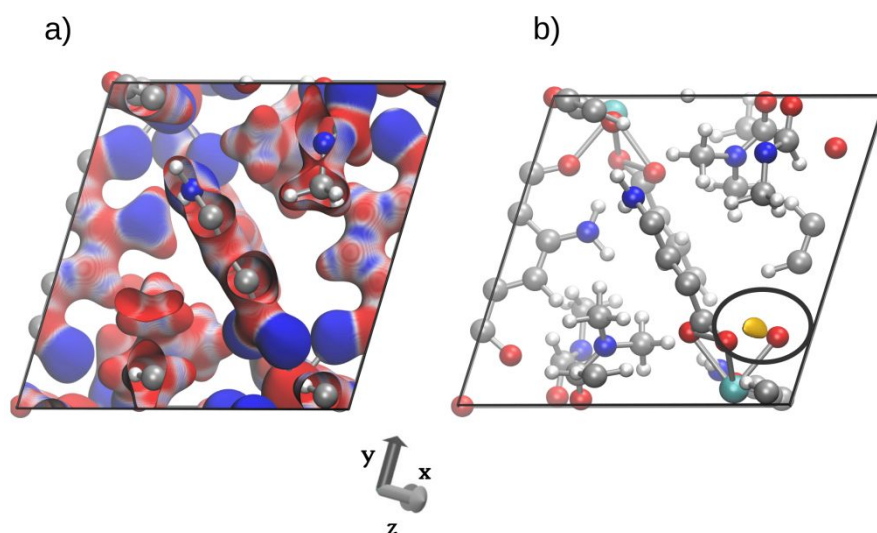
a)   b)

Figure S23. a) Electrostatic potential map plotted on the isovalue of the charge density of 0.07 electrons/a.u.[3]. b) Pockets of highly negative potential where the positively charged N of NO_2 is inserted as guess (starting) location for the geometrical optimization.

Interestingly, for each configuration the binding energies in Tb and Eu-MOF are very similar, suggesting a binding mechanism dominated by the local environment i.e. the NH_2 and CH_3 groups, and a negligible effect of the Ln atoms.

Charge transfer

In all cases, the binding results in a charge transfer from the MOF to the guest molecule. The amount of charge transfer is computed using Bader analysis and the results are reported in **Table S5**.

ConFigure	1	2	3	4	5	6	7	8
(Eu-MOF) Bind. En (eV)	0.48	0.37	0.53	0.45	0.54	0.50	0.40	0.51
(Eu-MOF) Ch. tr. (el)	0.540	0.570	0.676	0.378	0.539	0.599	0.503	0.516
(Tb-MOF) Bind. En (eV)	0.50	0.37	0.57	0.44	0.56	0.52	0.40	0.51
(Tb-MOF) Ch. tr. (el)	0.536	0.579	0.686	0.382	0.543	0.606	0.523	0.510

Table S5. Binding energies (eV) and charge transfer (electrons) for the Tb-MOF and Eu-MOF bound to NO_2.

The large charge transfer result in a modification of the bond angle ONO which is found to correlate linearly with the amount of charge transfer (**Figure S24**).
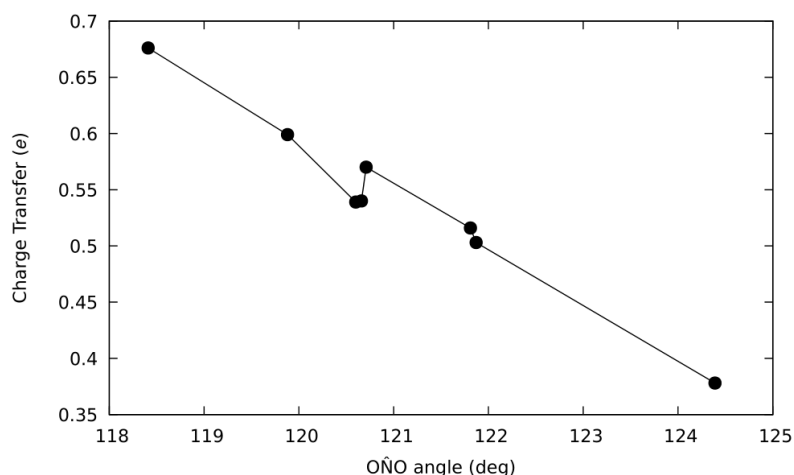
Figure S23. Charge transfer versus ONO bond angle for the 8 configurations computed in Eu-MOF.

The charge transfer is found to localize mostly on the three amines and to minor extent on the DMF molecules and negligibly on the Ln atoms. In **Table S6** we report the distribution of the charge transfer for configuration 3 and 5 in the case of Eu-MOF (for Tb-MOF the results is expected to be the same), i.e. those exhibiting the largest values of charge transfer.

	Ligand1	**Ligand2**	**Ligand3**	**DMF1**	**DMF2**	**DMF3**	**Ln1**	**Ln2**
ConFigure3	0.248	0.162	0.225	0.013	0.010	0.008	0.004	-0.003
ConFigure5	0.237	0.096	0.178	0.007	0.006	0.142	-0.005	-0.003

Table S6. Charge transfer distribution (in *electrons*) upon NO_2 binding for conFigure 3 and 5 computed for Eu-MOF. The primitive cell contains 3 amines, 3 DMF molecules and 2 Ln atoms.

The binding configuration number 3 is shown in **Figure S25** with the name of the ligands explicitly written.
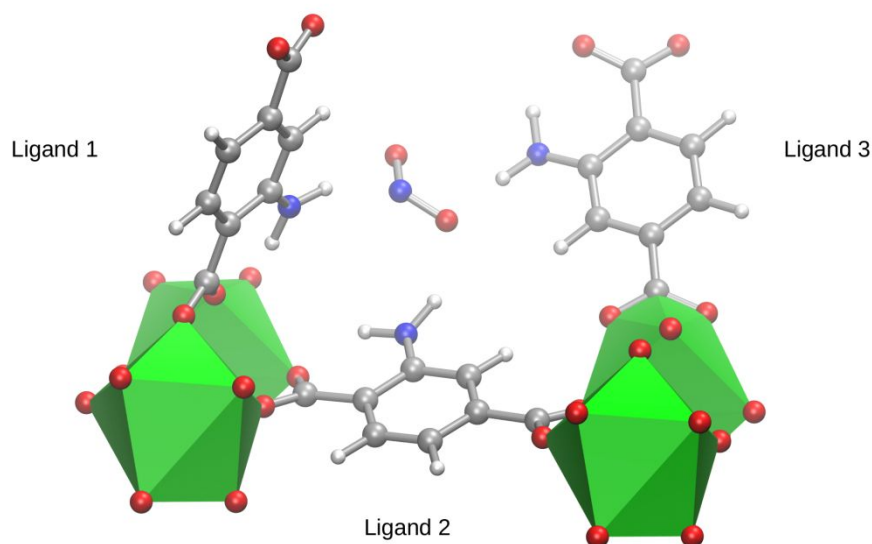

Figure S25. Binding configuration number 3. Only the three ligands within the primitive cell are shown for clarity.

Excited states calculations

The geometrical optimization of the complex ligand bound to NO_2 was optimized with the PBE+D functional using the nwchem [7] package using and a aug-cc-pvtz basis. The optimized configuration is shown in **Figure S26**.

Since we have shown that the NO_2 binding in the MOF proceeds via multiple H-bondings with the amino groups of the neighbouring ligands, we find it reasonable to give an estimate of the change in energy of the triplet state of the ligand using a cluster approach by taking only the ligand in its acidic form (LH). The triplet state of the ligand is computed using vertical transition energies. However, since it has been shown that the absolute position of the first triplet state of the similar ligands coordinated to Tb differs from its acid complex [8], we proceed in the following way: we compute the shift of the triplet state

of LH as a function of the binding distance with NO_2 by progressively displacing NO_2 far from the ligand along the H-bond direction; then, in order to get the triplet state of the ligand alone, we extrapolate the value for an infinite distance of guest molecule. Finally, in order to assist the experiments, we apply this shift to the experimentally determined level of the triplet state in Gd-MOF in order to provide an estimate of the shift of triplet state of the ligands of the MOFs, upon binding.

CASSCF/CASPT2

The CASSCF/CASPT2 calculations of the ligand-NO_2 complex were performed using the BAGEL code [9] with cc-pvtz basis set. In order to avoid intruder states CASPT2 was performed using a 0.4 a.u. level shift. **In order to compute the triplet state of the ligand, the doublet ground state and the first quartet states of the whole complex are computed to account for the unpaired electron of NO_2.** However, both here and in the main text we refer to this first excited quartet state as triplet state, for clarity, since NO_2 is not involved vide infra).
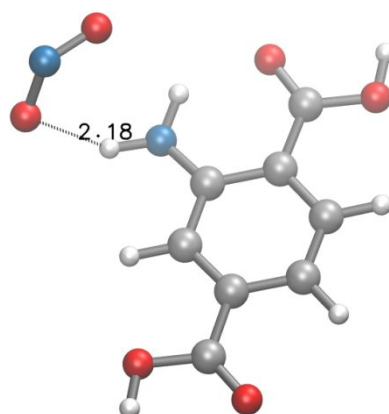

Figure S26. Optimized (DFT) configuration of the ligand bound to NO_2. The interaction proceeds via H-bond with a distance of 2.18 Å.

We employ an active space of 7 electrons in 10 orbitals. The 10 orbitals consist of 8 orbitals for the ligand and 2 for NO_2. The triplet state (quartet for the complex LH-NO_2) is predicted to be 2.745 eV with a dominant π-to-π* contribution. The largest CI coefficient (for this configuration) is 0.95, then the second largest coefficient drops to 0.07and it corresponds to a double excitation from the phenyl π to π* (see **Figure S24**). This state progressively shifts to higher energies as the guest molecule is displaced far from the ligand (see **Figure S25**, upper panel). When extrapolating the value to very large distances (infinity) we obtain a value of 2.777 eV leading to a decrease in energy of 0.03 eV. Notably, **Figure S25** also shows the linear correlation between this electronic excitation and the charge transfer computed as a function of the binding distance. At each configuration the charge transfer is computed using DFT and ESP charges. Since within the MOFs, the ligands are found to exhibit larger charge transfer than what we compute in the LH-NO_2 complex, the linear regression allows us to estimate the shift of T_1 in the MOF to range from 230 to 410 cm^{-1}.
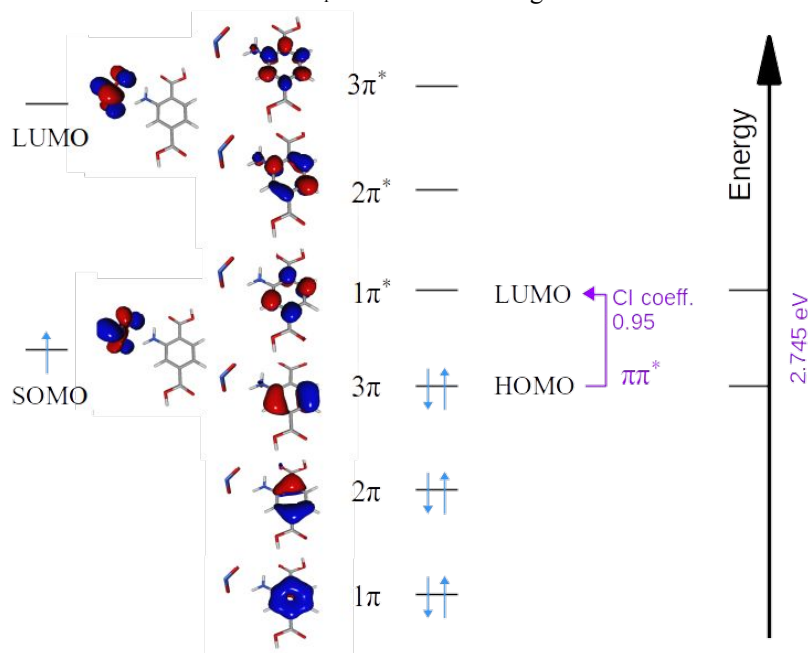

Figure S27. Molecular orbitals of the LH+NO_2 complex optimized using CASSCF with an active space of (7e, 10o).
The first triplet excited state at 2.745 eV consists of a π to π* excitation.

We also computed the triplet, T_1, (2.85 eV) and singlet, S_1, (3.59 eV) states of the ligand alone, in absence of NO_2 using a (6e, 8o) active space and a cc-pvtz basis set, which are in very good agreement with the experimental value. Although the comparison between the energy of the two sets of calculations (w and w/o guest molecule) is less trustworthy than the displacement strategy due to the different active space employed, these calculations helped confirm that the character for the T1 excitation is maintained while this is not the case for the S1. Specifically, we find the S1 in the LH+NO2 complex to have a charge transfer character from NO_2 to the ligand while S_2 and S_3 exhibit large mixings of charge transfer and π to π* excitations.

In order to test the accuracy of the above calculations, a larger active space of (13e, 13o) was employed using cc-pvdz basis set. We performed calculations for the Ln^+NO_2 complex at the binding configuration and a displacement of 0.6 Ang. Although the energy of the triplet is slightly larger than the previous case, i.e. 3.05 eV (versus 2.85 eV for the (7e, 10o) in double zeta), both the character of the excitation and the decrease in the triplet upon binding are confirmed.
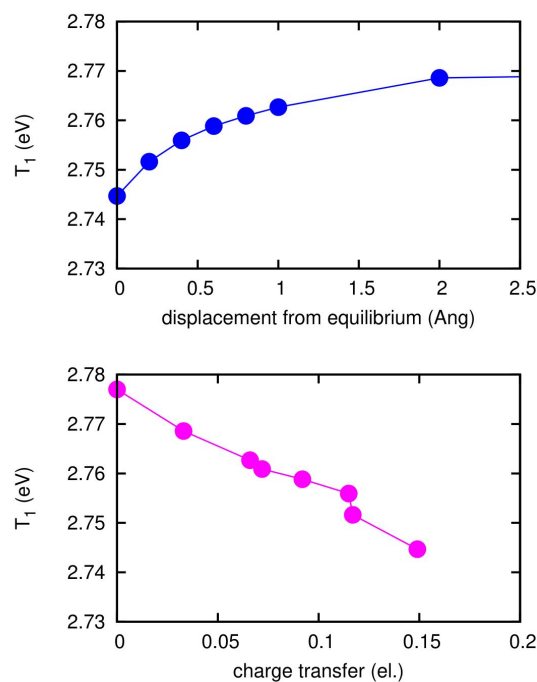

Figure S28. Triplet state energy as a function of the NO_2 displacement from its equilibrium position (see Figure S22) (upper panel) and as a function of the charge transfer from the ligand.

Sec 12 References

(1) Giannozzi, P.; Baroni, S.; Bonini, N.; Calandra, M.; Car, R.; Cavazzoni, C.; Ceresoli, D.; Chiarotti, G. L.; Cococcioni, M.; Dabo, I.; et al.. Quantum espresso: a modular and open-source software project for quantum simulations of materials. *J. Phys: Condens. Matter*, **2009**, *21* (39), 395502.

(2) Hamada. I. Van der Waals density functional made accurate. *Phys.Rev. B* **2014**, *89*, 121103-1–121103-5.

(3) Dion, M.; Rydberg, H.; Schroder, E.; Langreth, D. C.; Lundqvist, B. I. Van Der Waals Density Functional for General Geometries. Phys. Rev. Lett. 2004, 92, 22–25.

(4) Lee, K.; Murray, É. D.; Kong, L.; Lundqvist, B. I.; Langreth, D. C. Higher-Accuracy van Der Waals Density Functional. Phys. Rev. B - Condens. Matter Mater. Phys. 2010, 82 (8), 3–6.

(5) Black, C. A.; Fu, W. T.; Massera, C.; Roubeau, O.; Teat, S. J.; Aromı, G.; Gamez, P.; Reedijk, J. 3-D Lanthanide Metal-Organic Frameworks : Structure , Photoluminescence , and Magnetism. *Inorg. Chem.* **2009**, *48* (3)**,** 1062–1068.

(6) Poloni, R.; Smit, B.; Neaton. J.B. Ligand-assisted enhancement of CO_2 capture in metal-organic frameworks. *J. Am. Chem. Soc.* **2012,** *134*, 6714-6719.

(7) Valiev, M.; Bylaska, E. J.; Govind, N.; Kowalski, K.; Straatsma, T.P.; Van Dam, H. J. J.; Wang, D.; Nieplocha, J.; Apr_a, E.;. Windus, T. L.; DeJong, W. A. Nwchem: A comprehensive and Scalable open-source solution for large scale molecular simulations. *Computer Physics Communications* **2010**, *181*, 1477-1489.

(8) Gutierrez, F.; Tedeschi, Ch.; Maron, L.; Daudey, J.; Poteau, R.; Azema, J.; Tisnes, P.; Picard. C. Quantum chemistry-based interpretations on the lowest triplet state of luminescent lanthanides complexes. part 1. relation between the triplet state energy of hydroxamate complexes and their luminescence properties. *Dalton Trans.* **2004**, 1334-1347.

(9) Shiozaki, T. Bagel: Brilliantly advanced general electronic-structure library-modular and open-source software project for quantum simulations of materials. *WIREs COmput. Mol. Sci* **2018,** *8*:e1331.

Author Contributions

Arturo Gamonal, Chen Sun, A. Lorenzo Mariano have contributed equally in this work.